Microwave Remote Sensing of the Temperature and Distribution of Sulfur Compounds in the Lower Atmosphere of Venus

Jon M. Jenkins

SETI Institute/NASA Ames Research Center, MS 245-3, Moffett Field, California 94035
E-mail: jjenkins@mail.arc.nasa.gov

Marc A. Kolodner

Johns Hopkins University/Applied Physics Laboratory, Laurel, Maryland 20723-6099

Bryan J. Butler

National Radio Astronomy Observatory, P.O. Box O, Socorro, New Mexico 87801

Shady H. Suleiman

TRW, One Space Park, Redondo Beach, California, 90278

and

Paul G. Steffes

School of Electrical and Computer Engineering, Georgia Institute of Technology, Atlanta, Georgia 30332-0250

A multi-wavelength radio frequency observation of Venus was performed on April 5, 1996, with the Very Large Array to investigate potential variations in the vertical and horizontal distribution of temperature and the sulfur compounds sulfur dioxide (SO_2) and sulfuric acid vapor ($H_2SO_4(g)$) in the atmosphere of the planet. Brightness temperature maps were produced which feature significantly darkened polar regions compared to the brighter low-latitude regions at both observed frequencies. This is the first time such polar features have been seen unambiguously in radio wavelength observations of Venus. The limb-darkening displayed in the maps helps to constrain the vertical profile of $H_2SO_4(g)$, temperature, and to some degree SO_2. The maps were interpreted by applying a retrieval algorithm to produce vertical profiles of temperature and abundance of $H_2SO_4(g)$ given an assumed sub-cloud abundance of SO_2. The results indicate a substantially higher abundance of $H_2SO_4(g)$ at high latitudes (above 45°) than in the low-latitude regions. The retrieved temperature profiles are up to 25 K warmer than the profile obtained by the Pioneer Venus sounder probe at altitudes below 40 km (depending on location and assumed SO_2 abundance). For 150 ppm of SO_2, it is more consistent with the temperature profile obtained by Mariner 5, extrapolated to the surface via a dry adiabat. The profiles obtained for $H_2SO_4(g)$ at high latitudes are consistent with those derived from the Magellan radio occultation experiments, peaking at around 8 ppm at an altitude of 46 km and decaying rapidly away from that altitude. At low latitudes, no significant $H_2SO_4(g)$ is observed, regardless of the assumed SO_2 content.

This is well below that measured by Mariner 10 (Lipa and Tyler 1979, *Icarus* **39**, 192–208), which peaked at ~14 ppm near 47 km. Our results favor ≤100 ppm of SO_2 at low latitudes and ≤50 ppm in polar regions. The low-latitude value is statistically consistent with the results of Bézard *et al.* (1983, *Geophs. Res. Lett.* **20**, 1587–1590), who found that a sub-cloud SO_2 abundance of 130 ± 40 ppm best matched their observations in the near-IR. The retrieved temperature profile and higher abundance of $H_2SO_4(g)$ in polar regions are consistent with a strong equatorial-to-polar, cloud-level flow due to a Hadley cell in the atmosphere of Venus. © 2002 Elsevier Science (USA)

Key Words: Venus, atmosphere; atmospheres, composition, structure; radio observations; radiative transfer.

1. INTRODUCTION

The atmosphere of Venus continues to provide a unique laboratory for those researching atmospheric dynamics, chemistry, and climatology. Unlike the Earth, much of the latitudinal, zonal, and vertical motion in the Venus atmosphere is driven by variations in the solar energy absorption by its sulfuric acid clouds. The most pronounced global dynamical feature on Venus is the zonal retrograde superrotation of the upper atmosphere. While the planet rotates very slowly (225-day period), the upper atmosphere rotates westward at a much faster rate (5-day period). Although this feature has been readily characterized in ultraviolet

photographs of Venus by spacecraft such as Mariner 10 and Pioneer Venus Orbiter (PVO), it is not fully understood. It has been suggested (see, e.g., Rossow *et al.* 1980, Limaye *et al.* 1982) that the upper atmospheric superrotation could be maintained in part by a mean meridional flow such as a Hadley cell, which transports both heat and westward zonal angular momentum to the poles at the cloud tops. While there is certainly evidence for the existence of a cloud-level Hadley cell (Rossow *et al.* 1980, Limaye *et al.* 1982), specific characteristics such as the number of cells, the degree of its polar extension, and the altitude level of the equatorward return branch are not well known.

One way to identify important features of such a Hadley cell is to examine its impact on the abundance and distribution of sulfur compounds below the cloud layer. In particular, the characterization of the spatial variations in the temperature profile and sulfuric acid vapor ($H_2SO_4(g)$) can provide insight into the dynamical processes of the Hadley cell. According to the cloud particle cycle described by Knollenberg and Hunten (1980), and extended by Krasnopolsky and Pollack (1994) and by James *et al.* (1997), sulfuric acid is produced photochemically in a thin layer near 62 km. Diffusion and sedimentation carry the H_2SO_4 particles downward to form the middle and lower cloud layer. The lower cloud layer, however, is in equilibrium with the vapor layer directly beneath it, and its content is controlled by the upward flux of vapor. Likewise, downwelling or sedimentation can remove the lower cloud material by evaporation of the particles in the hotter sub-cloud environment, enhancing the abundance of vapor. Thus, regions of upwelling should feature a narrow layer of $H_2SO_4(g)$ at the base of the lower cloud, while regions of downwelling should exhibit an $H_2SO_4(g)$ layer extended farther beneath the cloud base. The global circulation plays an important role in cloud formation, too, as Imamura and Hashimoto (1998) point out. At mid and low latitudes the particles in the upper cloud are transported to the poles via the Hadley cell before there is time for sedimentation to carry the particles to the lower cloud. At high latitudes where the meridional wind is slow, the lower cloud can form by particles carried downward by sedimentation, diffusion, or the downward branch of the Hadley cell. From the high latitudes, the return flow of the Hadley cell transports $H_2SO_4(g)$ equatorward, which subsequently forms the lower cloud at mid and low latitudes by condensation via updrafts. Knowledge of the distribution of these sulfur compounds can also aid in understanding the thermochemical processes which constrain the abundances of other trace gases in the atmosphere of Venus such as sulfur trioxide (SO_3), carbon monoxide (CO), carbonyl sulfide (OCS), and water vapor (H_2O).

A useful technique for probing spatial variations in temperature and sulfur compounds in the atmosphere of Venus is the radio occultation. Over the past 30 years, such experiments have been conducted with several spacecraft. Two radio occultation profiles were obtained (at approximately 30°N and 30°S latitude) in 1967 by Mariner 5 (see, e.g., Fjeldbo and Kliore 1971), and an equatorial occultation profile was obtained in 1974 by Mariner 10 (Howard *et al.* 1974). Dozens of equatorial, mid-latitude, and

polar occultation profiles were obtained in the late 1970s and 1980s by PVO (see, e.g., Kliore and Patel 1980, Jenkins and Steffes 1991). Several radio occultation profiles spanning latitudes from 49° to 88° in either or both hemispheres were obtained in the early 1990s by the Magellan spacecraft (Jenkins *et al.* 1994, Hinson and Jenkins 1995, Jenkins and Hinson 1997). In addition, radio occultations were performed by Venera 9 and Venera 10 (see, e.g., Kolosov *et al.* 1979) and by Veneras 15 and 16 (see, e.g., Matyugov *et al.* 1990, Yakovlev *et al.* 1991).

All of the NASA experiments were performed at frequencies of 2.3 and 8.4 GHz with the exception of the Mariner 5 and later PVO experiments, which did not take data at 8.4 GHz. These experiments indicated that there was significant excess opacity below the main cloud over that due to the background CO_2/N_2 atmosphere, which is principally due to the microwave absorption of $H_2SO_4(g)$ (Steffes and Eshleman 1981). Moreover, the absorptivity profiles tend to vary with latitude (see, e.g., Jenkins and Steffes 1991), which indicates the existence of spatial variations in the distribution and abundance of $H_2SO_4(g)$. Thermochemical models of the lower atmosphere of Venus by Krasnopolsky and Pollack (1994) imply that the sub-cloud $H_2SO_4(g)$ thermally dissociates with decreasing altitude into sulfur trioxide and water vapor between 35 and 40 km above the surface. The SO_3 then reacts with carbon monoxide to produce additional carbon dioxide (CO_2) and sulfur dioxide (SO_2). This would suggest a (weak) anticorrelation between variations in the abundances of H_2SO_4 vapor and SO_2 in the lower atmosphere of Venus.

To confirm the existence of spatial variations in the abundances of sulfur compounds in the lower atmosphere of Venus, we performed a dual-frequency (14.94 and 22.46 GHz) radio observation of the planet with the NRAO Very Large Array (VLA). The frequencies were chosen because of their sensitivity to strong microwave absorbers at altitudes between 10 and 50 km in the atmosphere of Venus. A general description of this observation, as well as additional VLA observations of Venus near 1.4, 4.9, and 8.4 GHz, is presented in a related paper (Butler *et al.* 2002). This other paper focuses on the data collection and calibration issues as well as the modeling techniques required to obtain and interpret the disk-averaged brightness temperatures of Venus, especially at longer wavelengths.

In this paper, we focus on the methods and techniques required for the generation and proper interpretation of the emission maps of Venus obtained at 14.96 and 22.46 GHz. We derive best-fit model maps to the observed maps by varying the vertical profiles of $H_2SO_4(g)$, $q_{H_2SO_4}(z)$, and temperature, $T(z)$, for a given vertical profile of SO_2 ($q_{SO_2}(z)$—determined completely by a sub-cloud SO_2 abundance) in different regions of the planet. We do not attempt to vary all three profiles simultaneously, because the effects of $q_{SO_2}(z)$ cannot be uniquely separated from the effects of $T(z)$. The inseparability of these two quantities results from the fact that the frequency dependence of the absorptivity due to SO_2 is the same as that for the background CO_2/N_2 atmosphere except at very low pressures. For our purposes, the

TABLE I
**Summary of Measurements of Sulfur-Bearing Compounds
in the Venus Atmosphere at Low Latitudes**

Wavelength of observation	$H_2SO_4(g)$ abundance (ppm)	Sub-cloud SO_2 abundance (ppm)	Temperature profile[a]	Reference
2.45 μm	—	130 ± 40	Venus I[b]	Bézard et al. (1993)
2.45 μm	—	180 ± 70	COSPAR[c]	Pollack et al. (1993)
1.3–3.6 cm	<5	40	PV sounder[d]	Steffes et al. (1990)
1.3–21 cm	1–2.5	≤ 50	Mariner V[e]	Butler et al. (2002)
1.3, 2 cm	≤ 2.5	≤ 100	Retrieved[f]	This investigation

[a] With respect to the COSPAR equatorial model profile below 40 km, the Mariner V profile is 17 K warmer on average, the PV sounder profile is 6 K cooler on average, and the Venus I model is 3 K cooler on average.

[b] A model given by Seiff (1983) based on PV measurements for the lower atmosphere at latitudes less than 40°.

[c] The equatorial profile from the COSPAR international reference atmosphere model (Seiff et al. 1986).

[d] That measured by the PV sounder probe (Seiff et al. 1980).

[e] The temperature model of Muhleman et al. (1979), derived by extending the warmer radio occultation profile from Mariner 5 to the surface via a dry adiabat.

[f] Similar to the COSPAR equatorial model profile for $q_{SO_2} = 100$ ppm.

variation in the retrieved profiles as functions of SO_2 abundance represents a systematic uncertainty in the results. To investigate the statistical uncertainties, we also performed Monte Carlo calculations and used the approach of Rodgers (1990) to assess the vertical resolution of the retrieved profiles.

A number of ground-based observers have reported sub-cloud abundances of SO_2 from as low as 40 ppm to as high as 200 ppm. Table I contains a summary of the results for SO_2 and $H_2SO_4(g)$ from several ground-based near-infrared (NIR) and microwave observations of Venus. Pollack et al. (1993) reported 180 ± 70 ppm for the abundance of SO_2 near 42 km from NIR observations made near 2.45 μm. More sensitive measurements by Bézard et al. (1993) yielded 130 ± 40 ppm. In contrast to the NIR observations the microwave observations inferred significantly lower sub-cloud abundances of SO_2. Steffes et al. (1990) and Butler et al. (2002) reported values of $\sim$40 ppm based on multi-wavelength microwave observations of Venus from 1.3 to 3.6 cm and from 1.3 to 20 cm, respectively. As noted in Table I, the temperature profiles used by Pollack et al. (1993), Bézard et al. (1993), and Steffes et al. (1990) differed from each other by up to ± 5 K, while that used by Butler et al. 2002 was up to $\sim$26 K warmer than the coolest profile (used by Steffes et al. 1990), based on the Pioneer Venus (PV) sounder probe measurements. The results at low latitudes reported in this paper support a retrieved temperature profile similar to the COSPAR equatorial model for a sub-cloud SO_2 abundance of 100 ppm. This is statistically consistent with the NIR results. At higher latitudes, our results support a much lower sub-cloud abundance of SO_2, <50 ppm, to maintain consistency with temperature profiles retrieved by Magellan spacecraft radio occultation studies (Jenkins et al. 1994). Higher peak sub-cloud SO_2 abundances could be achieved for an SO_2 profile that decreased below 42 km. Such

a profile was reported by Bertaux et al. (1996) from measurements made with the ISAV-1 ultraviolet spectrometer on board an entry probe released from the VEGA-1 spacecraft. No plausible mechanism supporting a gradient in the sub-cloud SO_2 abundance has been identified, however.

The paper is organized as follows: First the observations are summarized and the brightness temperature maps are presented, following which a radiative transfer model used to analyze the measurements is described. This RTM is used in conjunction with a retrieval algorithm to extract vertical profiles of $H_2SO_4(g)$, $q_{H_2SO_4}(z)$, and temperature, $T(z)$, of the atmosphere of Venus, as functions of the assumed sub-cloud SO_2 content, from three different regions of the brightness temperature maps. We discuss the retrieved profiles for each of these regions: eastern equatorial, northern low latitude, and southern high latitude. We discuss the results in the context of other observations and then close with conclusions and suggestions for future work. Appendix A describes the retrieval algorithm used to obtain the temperature and $H_2SO_4(g)$ abundance profiles, while Appendix B describes in detail our estimates of the resolution and uncertainties of the retrieved profiles. Finally, Appendix C sketches a few of the numerical approaches used to accelerate the computations required for this investigation.

2. DUAL-FREQUENCY RADIO OBSERVATION OF VENUS

2.1. Observation Description

On April 5, 1996, a dual-frequency microwave observation of Venus was performed using the VLA of the National Radio Astronomy Observatory. The VLA interferometer is a collection of twenty seven 25-m radio antennas, which are distributed along tracks in a Y-shape on the plains of San Augustin, New Mexico. The VLA was in its "C-configuration," with maximum physical antenna separation of $\sim$3 km. All four Stokes parameters were measured in two 46-MHz passbands. This provides an equivalent bandwidth of 92 MHz when the two passbands are averaged together, and Stokes I is formed (Butler et al. 2002). The electronics were tuned to 14.94 and 22.46 GHz, alternating between the two frequencies throughout the observation. Quasar 3C286 and Quasar 3C48 were observed as primary calibrators, while radio source $0403 + 260$ served as the secondary calibrator. During the observation, Venus was a distance of $\sim$0.6735 AU from the Earth, resulting in an apparent size of 25.18 arcsec. The orientation of the planet and the position of the evening terminator during the VLA observation are shown in Fig. 1; the sub-Earth point on the Venus disk was $-4.6°$ latitude and 214.6° longitude, with a north pole position angle of $-12.4°$.

The actual quantity measured by a complex interferometer like the VLA is a sampling of the complex visibility function at the positions of the baselines between each of its antennas. The visibility function is the two-dimensional (2-D) Fourier transform of the sky brightness distribution (Thompson et al. 2001). In the case of planetary observations, the expected visibility function is close to a modified Bessel function as a function
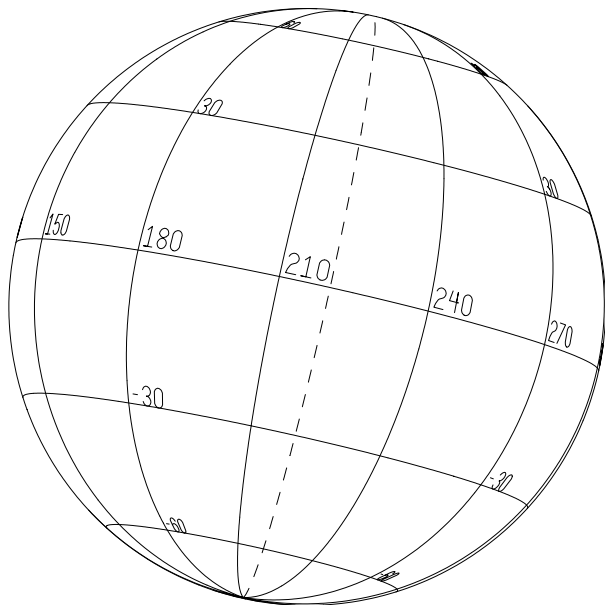
FIG. 1. The orientation of Venus during the observation. The sub-Earth point on Venus was 214.6° longitude and −4.6° latitude, with a north pole position angle of −12.4°. The Sun direction is to the right, with the terminator indicated by the dashed line.

of projected antenna spacing (Butler and Bastian 1999). The individual samples of the visibility function are referred to as "visibilities." The initial calibration of the visibilities obtained during our observations is described in more detail in Butler *et al.* (2002). We performed two further steps in calibrating the observed visibilities for this study: a self-calibration solution including amplitude correction (but constrained to not change the total measured flux density), and another based not on antennas, but on baselines. The baseline-based self-calibration calibrates out small baseline-related errors which are not corrected by the normal self-calibration process. Both of these additional calibrations are necessary to construct maps of high dynamic range (Cornwell and Fomalont 1999, Perley 1999).

2.2. Brightness Temperature Maps

We constructed maps of the received flux density following the prescription of Butler and Bastian (1999): (1) We fit a limb-darkened disk model to the visibilities; (2) we used that model as the starting point for the deconvolution (via the CLEAN algorithm— Högbom 1974, Clark 1980) by effectively subtracting that model from the visibilities; (3) we CLEANed to convergence with finite support—allowing CLEAN components to be found only within a circle with radius equal to the projected radius of the planet plus one full width (as per T. Cornwell, personal communication). The result of this process is a map of the emission of Venus at both frequencies, in units of Jy/beam (1 Jy = 10^{-26} Wm^{-2} Hz^{-1}). During the CLEAN process, the final step is a convolution by a Gaussian kernel (called the "CLEAN beam"), which smooths out variations in the final map

which occur at high spatial frequencies (that are poorly sampled) in the visibility data (Cornwell *et al.* 1999). The width of this CLEAN beam is generally chosen to match that of the central lobe of the "dirty beam" (the 2-D Fourier transform of the antenna spacings or samples), and we followed this practice. The resulting FWHMs were 1.10 arcsec at 22.46 GHz and 1.5 arcsec at 14.94 GHz, and this is effectively the resolution of our maps. We then converted these flux density maps, $F(l, m)$, into brightness temperature maps, $T_b(l, m)$, via (Butler and Bastian 1999)

$$T_b(l, m) = F(l, m)\frac{\lambda^2}{2k_b}\frac{4\ln 2}{\pi\ FWHM^2} + T_{CMB}, \qquad (1)$$

where k_b is Boltzmann's constant, *FWHM* is the CLEAN beam full width at half maximum at wavelength l, and T_{CMB} is the cosmic microwave background temperature (2.7 K). The peak value in the resultant brightness temperature maps was 604.4 K at 14.94 GHz and 540.6 K at 22.46 GHz. The rms uncertainty in regions off the planet in the final maps was 0.66 K at 14.94 GHz and 1.1 K at 22.46 GHz. The rms uncertainty for on-planet pixels is slightly higher due to source self-noise, but Venus is not such a strong source that it will be significantly higher (Butler and Bastian 1999). The uncertainties in the overall flux density scale are ∼3% at 14.94 GHz and ∼5% at 22.46 GHz (R. Perley, personal communication).

2.3. Residual Brightness Temperature Maps

Although the resultant brightness temperature maps showed small variations, it was very difficult to see them because they were much smaller than the overall brightness temperature at both frequencies. To accentuate these variations, a simple azimuthal average was taken around the center of the planet, and this average was subtracted from the overall map. The resultant residual maps are shown in Fig. 2. These residual maps exhibit various features of interest, but the most prominent are the dark regions at high latitudes in both the north and south at both frequencies. This is likely due to cooler temperatures and/or higher abundances of trace microwave-absorbing constituents in the lower atmosphere in the polar regions. We note that the weighting functions at these frequencies peak near 15 and 24 km, due to thermal structure, and also near the cloud base, due to H_2SO_4(g) (see Fig. 3). The presence of polar features on Venus as inferred from interferometric radio wavelength observations was first suggested by Clark and Kuzmin (1965), who saw poles cooler than the equator by 25%. Later interferometric observations at a similar wavelength (near 11 cm) disputed this result and showed poles which were warmer than the equator by 16 K (Sinclair *et al.* 1972). Interferometric observations at a shorter wavelength (near 3.1 cm) showed no measurable polar features (Berge and Greisen 1969). All of these observations were at wavelengths longer than presented here, however, and so are much more sensitive to actual surface properties than atmospheric properties. Our data are the first, at any wavelength, to unambiguously show such polar features.
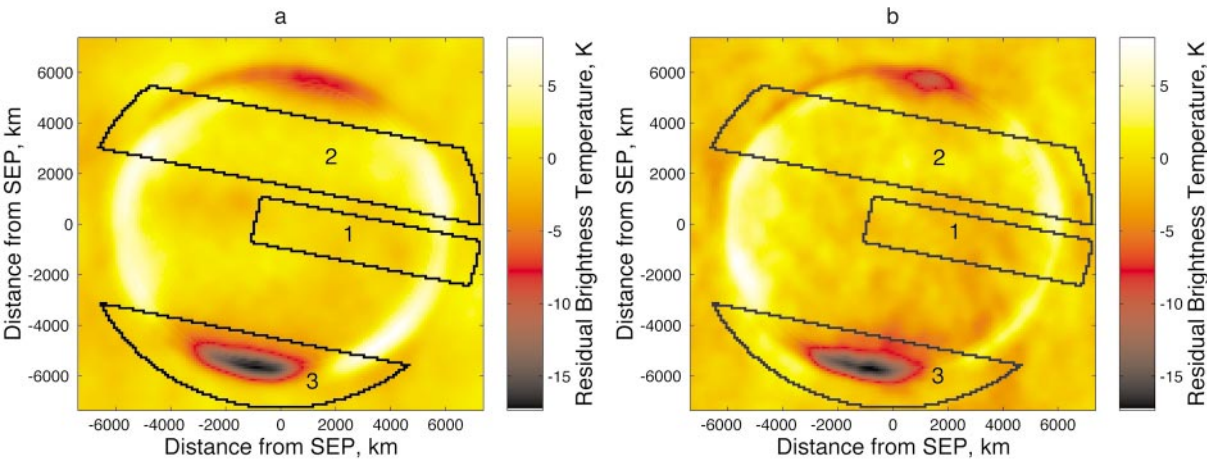
FIG. 2. Residual brightness temperature maps of Venus at (a) 14.94 GHz and (b) 22.46 GHz displayed in false color. The borders of the three regions for which retrievals of the temperature and $H_2SO_4(g)$ abundance profiles were performed are shown as well and labeled from 1 to 3 in the order in which they are discussed in the text. The residual maps were obtained by subtracting the azimuthal average from each pixel; i.e., the maps compare the brightness of each pixel with other pixels at the same angular distance from the sub-Earth point.

In addition to the dark polar features, the north hemisphere appears to be warmer than the equatorial region at latitudes between 10°N and 45°N. This is observed in the south hemisphere as well, although there is also an east–west asymmetry that is difficult to interpret with only a single set of maps. This asymmetry may be due to day–night variations in the abundances of SO_2 or $H_2SO_4(g)$ or in the temperature profile. The volcanic feature Maat Mons can be seen as a spot ∼5 K darker than its surroundings just above and to the left of the center of the 14.94-GHz residual map. It is slightly cooler than other regions at similar distances from the disk center because of its high elevation. (There is no emission contribution from the hot lower atmosphere, and the emission from the surface is reduced because the temperature there is cooler due to the lapse rate of the temperature in the atmosphere.)
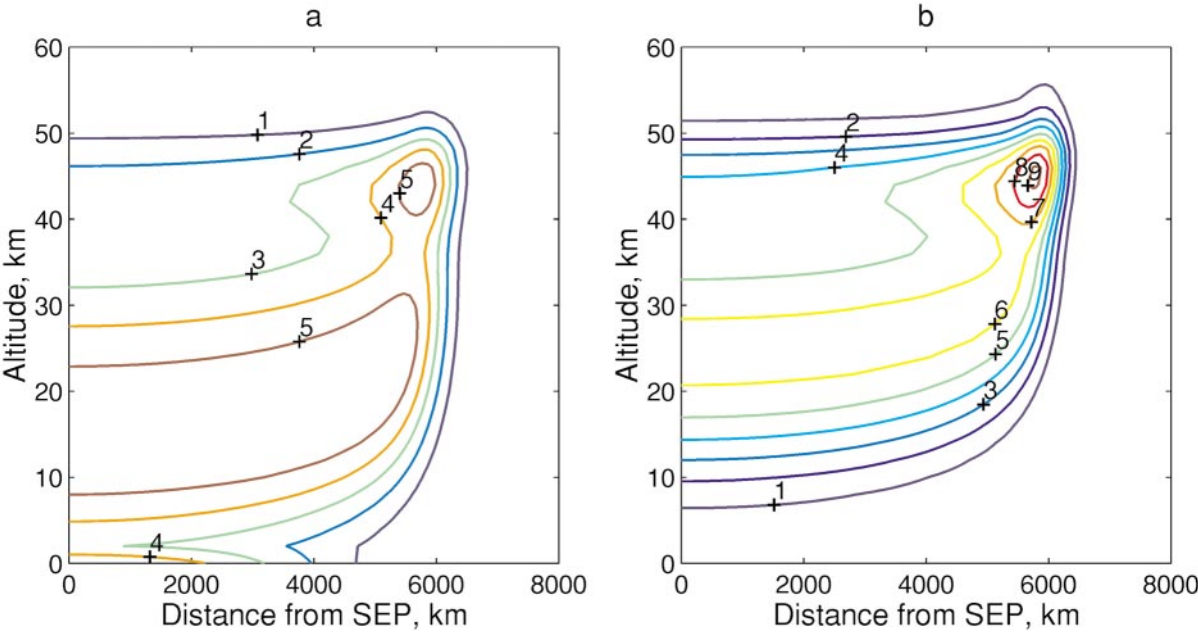

FIG. 3. Contour plots of the weighting functions for (a) 14.94 GHz and (b) 22.46 GHz as functions of altitude and distance from the sub-Earth point. The contours are labeled in percentage and include the effects of the finite resolution of the VLA maps (1.5 arcsec at 14.94 GHz and 1.1 arcsec at 22.46 GHz). The weighting functions were produced using the Pioneer Venus sounder probe PT profile and a peak $H_2SO_4(g)$ abundance of 5 ppm at 45 km altitude.

3. RADIATIVE TRANSFER MODELING

Further analysis and interpretation of the microwave brightness temperature maps discussed above require a radiative transfer model (RTM) appropriate for Venus that includes effects specific to the observed frequencies. This section describes such an RTM and the process of using a model atmosphere and that RTM to obtain a synthetic VLA map to compare with the actual maps. For a given model atmosphere, three steps are required to generate a synthetic brightness temperature map. First, the RTM is used to trace the trajectories of a large number of rays impinging upon the top of the atmosphere and obtain brightness temperature as a function of the impact parameter or normalized distance from the center of the planet, a, at each wavelength. (The one-dimensional model is a function only of a.) The resulting brightness temperature map is then adjusted to the resolution of the observed map by convolving it with the Gaussian CLEAN beam appropriate for the observing wavelength. The final model brightness temperature map is obtained from that map by correcting for the resolution of the planet by the individual interferometer elements (the antennas). The antenna voltage reception pattern is well approximated by a modified Bessel function as a function of a (Napier 1999). The correction is zero at $a = 0$, but it becomes a 1.3% decrease in brightness at 14.94 GHz and a 3% decrease in brightness at 22.46 GHz at the limb of the disk. The second and third steps in this process are well understood and relatively straightforward to implement. The RTM, however, is not quite so straightforward. Appendix C describes the methodology used to accelerate the computations to generate the required synthetic brightness temperature maps. The remainder of this section describes the RTM in detail.

The mean radius of the Venus surface is taken to be 6052 km and the layered atmosphere is extended 100 km above the surface, with 1-km layer width. The brightness temperature is computed at both observation frequencies by the RTM over a range of normalized impact parameters from 0 to 1 (physical impact parameters of 0 to 6152 km). Given a pressure–temperature (PT) profile, a mass density profile $\rho(z)$ is computed using the appropriate gas constant (0.00189 atm m³ kg⁻¹ K⁻¹) for an atmosphere of 96.5% CO_2 and 3.5% N_2. In addition, given the known concentrations and the density-normalized refractivity values of CO_2 and N_2 (Essen and Froome 1951), the refractivity profile $N(z)$ is computed from the density profile via a scalar multiple: $N = (251.09 \, \text{m}^3 \, \text{kg}^{-1}) \, \rho$. The refractive index profile, $n(z)$, is defined in terms of the refractivity via $n(z) = 1 \times 10^{-6} N(z) + 1$. This refractive index profile is used in calculating the refraction as the ray passes through the layers in the model atmosphere. Microwave absorption in the atmosphere of Venus at 15 and 22 GHz is dominated by the absorption from collisionally induced dipole moments of CO_2 and N_2 and is given by (Ho *et al.* 1996)

$$\alpha_{CO_2} = 1.15 \times 10^8 \left(q_{CO_2}^2 + 0.25 q_{CO_2} q_{N_2} + 0.0054 q_{N_2}^2 \right) f^2 p^2 T^{-5}, \quad (2)$$

where f is the frequency in GHz, p is the pressure in atm, T is the temperature in kelvins, q is the number mixing ratio (0.965 for CO_2 and 0.035 for N_2), and α is the absorption in units of dB km⁻¹. At least two other species in the atmosphere of Venus exhibit significant absorption at microwave wavelengths: SO_2 and $H_2SO_4(g)$. The opacity of SO_2 is modeled using the formalism of Suleiman *et al.* (1996), including 1587 lines of SO_2 below 750 GHz. For $H_2SO_4(g)$, we use the expression

$$\alpha_{H_2SO_4} = 55.874 \times 10^{-6} p^{1.08} (553/T)^3 f^{1.15} q_{H_2SO_4}, \quad (3)$$

where p is pressure in atm, f is the frequency in GHz, T is the temperature in kelvins, and $q_{H_2SO_4}$ is the abundance of $H_2SO_4(g)$ in ppm. This expression is slightly modified from that given in Kolodner and Steffes (1998) as per M. A. Kolodner (personal communication). Note that the effects from the sulfuric acid droplets and particles in the clouds are negligible at microwave frequencies (Fahd 1992).

The brightness B_ν' emanating from the planet at a particular microwave frequency and impact parameter a is computed using the radiative transfer equation

$$B_\nu'(a) = \varepsilon(\theta) B_{\text{surf}} e^{-\tau_{0\to\infty}} + [1 - \varepsilon(\theta)] B_{\text{CMB}} e^{-2\tau_{0\to\infty}}$$
$$+ \sum_{i=1}^{N} B_i (1 - e^{-\tau_i}) e^{-\tau_{i+1\to\infty}}$$
$$+ \sum_{i=1}^{N} B_i (1 - e^{-\tau_i})[1 - \varepsilon(\theta)] e^{-\tau_{0\to i-1}} e^{-\tau_{0\to\infty}}, \quad (4)$$

where B_{surf} is the surface brightness, B_i is the brightness of atmospheric layer i, B_{CMB} is the cosmic microwave background brightness (2.7 K in brightness temperature units), ε is the surface emissivity at emission angle θ (a function of a), and the terms containing τ (also functions of a) are opacities integrated along different sections of the ray path for impact parameter a. The brightnesses, B_{surf} and B_i, $i = 1, \ldots, N$, are related to the physical temperatures of the surface and the atmospheric layers by the Planck function. At the wavelengths considered here, the Rayleigh–Jeans approximation holds, and brightness is directly proportional to brightness temperature. The first term in Eq. (4) is the radiation emitted from the surface, attenuated by the atmosphere it passes through. The second term is cosmic background, attenuated by two passes through the atmosphere and a reflection from the surface. The third term represents the upwelling radiation emitted by each atmospheric layer, attenuated by the atmospheric absorption encountered on its way up out of the atmosphere. The final term is the downwelling radiation from each atmospheric layer, attenuated by the atmosphere beneath it, modified by the reflection off the surface, and finally, attenuated by the entire atmosphere on its upward path toward the VLA. The optical depth integrated along the (refracted) path

of the ray in each layer, $\tau_i(a)$, is given by

$$\tau_i(a) = \int_{s(z=z_i)}^{s(z=z_{i+1})} \alpha(s)\, ds. \qquad (5)$$

We note that the RTM accounts for refraction effects explicitly in Eq. (5) for all rays. The effective optical depth to the surface from the top of the atmosphere, $\tau_{\infty \to 0}$, is given by

$$\tau_{0 \to \infty}(a) = \sum_{i=1}^{N} \tau_i(a), \qquad (6)$$

while the optical depths $\tau_{0 \to i-1}$ and $\tau_{i+1 \to \infty}$ are sums of the individual layer optical depths from the surface to layer $i - 1$ and from layer $i + 1$ to the top of the atmosphere, respectively. Equation (5) applies to limb-sounding rays, too, if appropriate modifications of the opacities and surface emissivity are made.

To compute the surface emissivity ε, we first assume that the surface dielectric constant is uniform across the surface and has a value of $\epsilon_d = 4.0$ (Pettengill *et al.* 1992). The surface reflection coefficient for unpolarized radiation is the average of the Fresnel reflectivities for horizontally and vertically polarized radiation,

$$R_{\text{surf}}(\theta) = \frac{1}{2} \left[\frac{\cos\theta - \sqrt{\epsilon_d/n_1^2 - \sin^2\theta}}{\sin\theta + \sqrt{\epsilon_d/n_1^2 - \sin^2\theta}} \right]^2$$
$$+ \frac{1}{2} \left[\frac{\epsilon_d/n_1^2 \cos\theta - \sqrt{\epsilon_d/n_1^2 - \sin^2\theta}}{\epsilon_d/n_1^2 \cos\theta + \sqrt{\epsilon_d/n_1^2 - \sin^2\theta}} \right]^2 , \quad (7)$$

where θ is the transmission angle through the atmospheric layer directly above the surface, and n_1 is the index of refraction of the atmosphere above the surface. The surface emissivity is related to the reflectivity by $\varepsilon(\theta) = 1 - R_{\text{surf}}(\theta)$.

Equation (4) can be rewritten as

$$B_\nu'(a) = B_{\text{surf}} W_s(a) + B_{\text{CMB}}\, W_{\text{CMB}}(a) + \mathbf{W}_{\text{atm}}(a)^T \cdot \mathbf{B}, \quad (8)$$

where W_s is the surface weighting function, $\mathbf{W}_{\text{atm}}$ is the vector atmospheric weighting function, and W_{CMB} is the cosmic microwave background weighting function. These weighting functions determine the relative contributions from each radiation source. Figure 3 shows contour maps of the atmospheric and surface weighting functions (combined into one matrix) for the measurements made at the VLA at both 14.94 (Fig. 3a) and 22.46 GHz (Fig. 3b). These contour maps take the resolution of our maps into account and were generated for a PT profile matching the PV sounder probe profile, with 100 ppm of SO_2 below 48 km, and an abundance of $H_2SO_4(g)$ following a Gaussian profile peaking at 5 ppm at 45 km altitude with a FWHM of 9.25 km additionally constrained by the saturation vapor abundance determined by the PT profile. At impact parameters less

than 4900 km, the weighting functions peak at ~15 km for 14.94 GHz and at ~24 km for 22.46 GHz due to contributions from the temperature profile. Both also exhibit narrow peaks at ~44 km near the limb due to the sub-cloud H_2SO_4 layer. By combining measurements at different look angles and at both wavelengths, we are able to retrieve profiles of temperature and sulfuric acid vapor from the VLA maps. The combination of the uncertainties in the observed brightness temperatures and the shape of the 2-D weighting functions given in Fig. 3 determine the resolution and sensitivity of the atmospheric profiles derived from the microwave emission maps. These are discussed in the following section and in Appendix B.

4. RETRIEVALS OF KEY ATMOSPHERIC PROFILES

In this section we describe retrievals of profiles of temperature, $T(z)$, and $H_2SO_4(g)$, $q_{H_2SO_4}(z)$, and their associated uncertainties and vertical resolution. We then present retrievals from three different regions of the brightness temperature maps obtained at the VLA: (1) eastern equatorial, (2) northern low latitude, and (3) southern high latitude. Figure 2 shows the borders of the three regions superimposed on the residual emission maps.

4.1. Profile Retrievals, Uncertainty, and Resolution

The vertical profile retrievals were obtained using the algorithm presented in detail in Appendix A. We summarize the retrieval process here. In each region, the atmosphere is assumed to be radially symmetric; i.e., the temperature, pressure, and abundances of microwave absorbing gases are only allowed to vary with altitude. However, even if this assumption is not strictly valid, we note that the weighting functions of Fig. 3 imply that the $H_2SO_4(g)$ abundance determines most of the emission from the limb and that the thermal emission from below ~50 km is broadly weighted across the disk. Thus, while using a large number of pixels for a retrieval does increase the resolution of the resulting profiles somewhat, it mainly serves to decrease the stochastic errors on the resulting profiles. This approach contrasts with IR observations above 80 km, where each weighting function is furnished simply by a separate observing channel. For the neutral Venus atmosphere, however, the assumption of radial symmetry is valid with respect to the temperature profile below ~50 km as evidenced by the measurements of the PV probes (Seiff *et al.* 1980). The temperature profile does vary with latitude, with most of the variability occurring at high latitudes. It also appears to be a valid assumption with respect to $H_2SO_4(g)$, at least in some regions of the Venus atmosphere (Jenkins *et al.* 1994). We note also the duration of the VLA observations (12 h) during which the atmosphere rotated by some amount; consequently the resulting maps have been "smeared" from east to west.

As it is not possible to retrieve simultaneously the profile of SO_2 along with the profile of $H_2SO_4(g)$ and temperature, we assume that the sub-cloud abundance of SO_2 is uniform and

fixed below 48 km and decays exponentially above this level with a scale height of 3 km. Our approach is to vary the assumed sub-cloud abundance of SO_2 over the range of values reported in the literature (0 to 200 ppm; see Table I) and to study the resulting $T(z)$ and $q_{H_2SO_4}(z)$ profiles obtained over this range of q_{SO_2} values. We specify an initial profile of $T(z)$ and $q_{H_2SO_4}(z)$, then minimize the difference between the values of brightness temperature observed over some region of the maps by varying the values in these vertical profiles, subject to constraints as follows. The $H_2SO_4(g)$ profile must be non-negative and can be no greater than the saturation vapor abundance corresponding to the temperature of a given altitude. In addition, $q_{H_2SO_4}(z)$ is set to 0 ppm outside of the altitude interval from 30 to 60 km. The weighting functions for $T(z)$ are negligible above ∼75 km; thus we allow the retrieved temperature profile to vary from the initial profile only at or below this altitude.

We investigated the uncertainty in the retrieved vertical profiles with Monte Carlo simulations of the retrievals. The details of this analysis are given in Appendix B, along with the analysis of the vertical resolution of the retrieved profiles. For $T(z)$ the 68% confidence interval bound (corresponding roughly to a 1-σ uncertainty) is between −3 and +4 K everywhere except below 10-km altitude (see Fig. 9a). For $q_{H_2SO_4}$, the 68% confidence interval is between −2 and +3.5 ppm at all altitudes (see Fig. 9b). This analysis does not include the effects of the systematic errors in the absolute calibration scale for the VLA measurements. By independently adjusting the absolute scale of the two maps over the stated calibration uncertainty ranges, one derives temperature profiles that vary by several tens of kelvins and peak $H_2SO_4(g)$ abundances that range from 0 to 20 ppm. Thus, the conclusions we draw from these VLA maps depend critically on the calibration errors being highly restricted within the stated uncertainties (3 and 5% for 14.96 and 22.46 GHz, respectively).

In addition, we applied the theory developed by Rodgers (1976, 1990) to assess the resolution of the retrieved profiles. For $T(z)$ the vertical resolution is approximately 20 km while it is ∼12 km for the $H_2SO_4(g)$ retrievals. Another important result from this analysis is that the region of the atmosphere for which the thermal structure can be reliably determined from these observations lies between ∼5 and ∼50 km. The portions of the retrieved temperature profiles outside this interval provide smooth transitions to the initial "seed" profile but do not reveal actual atmospheric structure.

4.2. Eastern Equatorial Region

This region contains 1696 pixels spanning latitudes from 13.7°S to 7.8°N in a 4-arcsec-wide swath that is centered on the sub-Earth point (SEP) and extends 2 arcsec west of the SEP to 15 arcsec east of the SEP, well off the planetary limb (see Fig. 2). We chose the eastern portion of the equatorial region in order to exclude the Maat Mons complex, since the retrievals discussed here do not account for local topography and Maat Mons is identifiable in the 14.94-GHz map. Figure 4a shows

the brightness temperatures in this region as a function of ray impact parameter. The PT profile for the retrieval was initialized with that measured by the PV sounder probe Seiff *et al.* (1980), while the $H_2SO_4(g)$ profile was initialized to 0 ppm. We varied the abundance of SO_2 from 0 to 200 ppm in steps of 50 ppm, retrieving $T(z)$ and $q_{H_2SO_4}(z)$ for each value of q_{SO_2}. Figure 4b shows the residual fitting errors in brightness temperature between the model and the actual maps versus distance from the SEP, demonstrating the goodness of fit. The fits attained a $\chi^2 = 3056$ for an rms error of 0.95 σ per pixel. Figure 5a shows the difference between the retrieved temperature profiles and the initial profile, that of the PV sounder. The difference between the Mariner 5 occultation profile and the PV sounder profile is also shown for comparison. All retrieved temperature profiles are significantly warmer than the PV sounder probe profile below 20 km, increasing from 13 to 29 K as the assumed SO_2 abundance increases from 0 to 200 ppm. For $q_{SO_2} > 50$ ppm, $T(z)$ is warmer than the PV sounder profile between 25 and 50 km, and by as much as 14 K for 150 ppm of SO_2. It is interesting to note that as the assumed SO_2 abundance increases, the inferred temperature profiles move from better agreement with the PV sounder profile to agreement with the Mariner 5 occultation profile. The retrieved profile of $H_2SO_4(g)$ in this region is 0 ppm at all altitudes. The lack of $H_2SO_4(g)$ is discussed in Section 4.7.

4.3. Northern Low-Latitude Region

This region is a nearly rectangular swath 5 arcsec wide spanning latitudes from 9°N to 45°N and is composed of 4080 pixels. The southern and northern borders are 3 and 9 arcsec north of the SEP, respectively (see Fig. 2). The east and west edges of this region were truncated at distances of 15 arcsec. The minimum impact parameter in this region is 1496 km, within about three beamwidths of the SEP. This fact likely reduces the vertical resolution of the retrieved profiles somewhat in comparison with the equatorial retrievals. Given the greater number of pixels in this region, however, the stochastic errors in the retrieved profiles are likely somewhat smaller than those in the equatorial region. We chose this region in part because of the high degree of apparent symmetry that is lacking at similar latitudes in the south hemisphere. Figure 4c shows the brightness temperatures versus impact parameter for this region, and Fig. 4d shows the residual brightness temperature fitting errors between the maps and the model. For this region, $\chi^2 = 19,569$, for an rms error of 1.6 σ per pixel. While the fitting errors are comparable to those of the equatorial fit at impact parameters less than 4884 km from the SEP, there are significantly higher differences near the limb. This is most likely due to nonuniformity in limb-darkening evident in the western limb of this region. Regardless of this fact, the temperature profiles shown in Fig. 5b are quite similar to those retrieved for the equatorial region, although they are up to 6 K warmer between 25 and 40 km and up to 6 K cooler between 40 and 60 km and below 10 km. The difference between the Mariner 5 occultation profile and the PV sounder profile is shown here again for comparison. These profiles also exhibit a
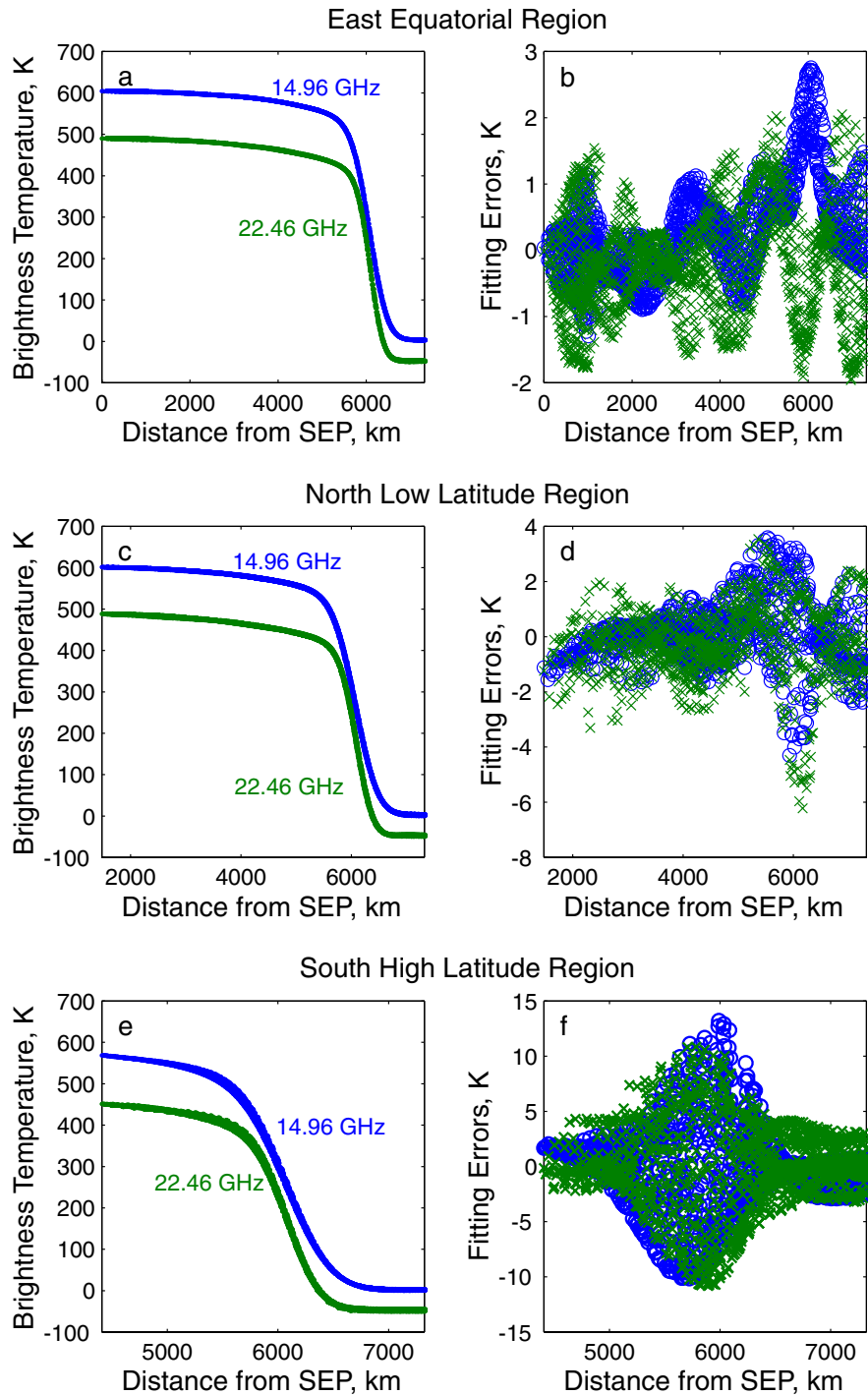
FIG. 4. Fitting the VLA brightness temperature maps. (a) Brightness temperatures at both 14.94 and 22.46 GHz for the eastern equatorial region in kelvins versus impact parameter. The points for 22.46 GHz have been displaced downward by 50 K. (b) Residual brightness temperature errors at 14.94 GHz (o's) and 22.46 GHz (x's) for the retrieved temperature profile for the eastern equatorial region. (c) Brightness temperatures at both 14.94 and 22.46 GHz for the northern low-latitude region in kelvins versus impact parameter. The points for 22.46 GHz have been displaced downward by 50 K. (d) Residual brightness temperature errors at 14.94 GHz (o's) and 22.46 GHz (x's) for the northern low-latitude region. (e) Brightness temperatures at both 14.94 and 22.46 GHz for the southern high-latitude region in kelvins versus impact parameter. The points for 22.46 GHz have been displaced downward by 50 K. (f) Residual brightness temperature errors at 14.94 GHz (o's) and 22.46 GHz (x's) for the southern high-latitude region. For clarity, only 1000 points were plotted for each wavelength in panels b, d, and f.
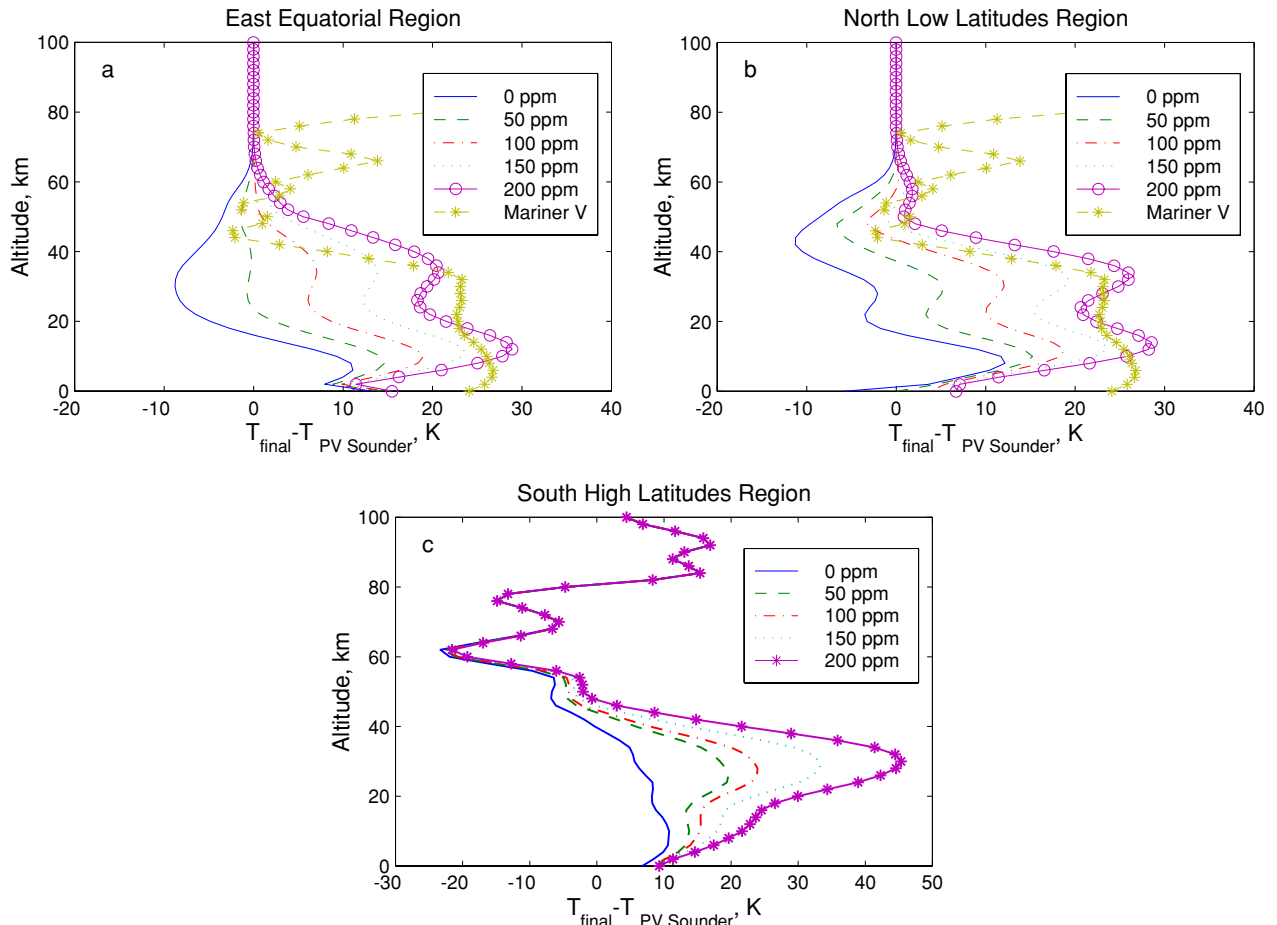
FIG. 5. Results of the analysis of the VLA brightness temperature maps. (a) The difference between the retrieved temperature profile for the eastern equatorial region and the initial assumed profile, that of the PV sounder probe, as a function of the assumed SO_2 abundance. The difference between the Mariner 5 occultation profile and the PV sounder profile is shown for comparison. (b) The difference between the retrieved temperature profile for the northern low-latitude region and the initial assumed profile, that of the PV sounder probe, as a function of the assumed SO_2 abundance. The difference between the Mariner 5 occultation profile and the PV sounder profile is shown for comparison. (c) The difference between the retrieved temperature profile for the southern high-latitude region and the PV sounder probe, as a function of the assumed SO_2 abundance. The initial temperature profile in this region was that obtained from the December 1992 Magellan Orbit 6369 radio occultation, extended below 34 km to the surface via a dry adiabat.

greater similarity with the PV sounder profile at low abundances of SO_2, moving toward the Mariner 5 occultation profile as SO_2 is added to the atmosphere. Here, as in the eastern equatorial region, the retrieved profile of $H_2SO_4(g)$ is 0 ppm for all altitudes (see Section 4.7).

4.4. Southern High-Latitude Region

This region is tangential to the 46.5°S latitude and extends east, west, and south to distances of 15 arcsec (see Fig. 2). The impact parameters for the 2509 pixels in this zone attain their minimum at 4408 km, where the weighting functions of Fig. 2 exhibit peaks near 20 and near 28 km. Thus, the retrieved profiles do not have as great a resolution as in the other two regions. Figure 4e shows the brightness temperatures versus ray impact parameter. The residual brightness temperature fitting errors,

shown in Fig. 4f, are significantly higher than those obtained in the lower latitude regions. For this region, $\chi^2 = 115,471$, for an rms error of 4.8 σ per pixel. This is not unexpected, however, as the range of latitudes is the largest in this region, and the largest range of variability evident in the residual maps of Fig. 2 occurs in this region. In addition, previous investigations of the atmosphere of Venus indicate that it is most variable at latitudes above 60° (Seiff *et al.* 1980). The profiles retrieved from this region, then, must be considered to be averages over the entire region. In contrast with the two other regions, the initial temperature profile was taken from the December 1992 Magellan Orbit 6369 radio occultation, extended below 34 km (the minimum altitude probed by the radio occultation) by assuming a static stability consistent with PV probe measurements (Seiff *et al.* 1980). The differences between the retrieved temperature profiles and the PV sounder profile are given in Fig. 5c.
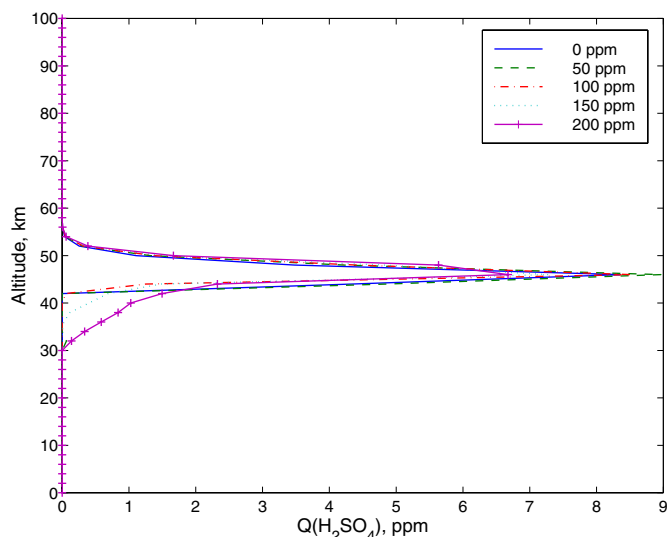
FIG. 6. The retrieved abundance profiles for $H_2SO_4(g)$ as a function of assumed SO_2 abundance for the southern high-latitude region.

FIG. 7. Retrieved temperature profiles from all three study regions for an SO_2 abundance of 50 ppm.

We note that the retrieved profiles are also significantly warmer below 50 km than the initial temperature profile. As the uncertainties in the temperature profiles from the radio occultation studies are much lower than those obtained in this study, we would argue for lower abundances of SO_2 (<50 ppm) at high latitudes for better agreement with the radio occultation studies.

In contrast to the low-latitude regions, significant amounts of $H_2SO_4(g)$ were retrieved in this region and are displayed in Fig. 6. The profiles attain peak values of 7–9 ppm at 46 km, decaying rapidly below 45 km, with the exception of the profiles based on 150 and 200 ppm of SO_2. These profiles decay more slowly than the other profiles. All these profiles are generally consistent with the radio occultation measurements made by the Magellan spacecraft at latitudes poleward of 45° (see, e.g., Jenkins and Hinson 1997, Kolodner and Steffes 1998), taking into account that the VLA-derived profiles are averages of the sulfuric acid vapor content over this entire region. One important observation is that the retrieved sulfuric acid vapor profile is not strongly dependent on the assumed abundance of SO_2. This implies that the principal effect of any uncertainty in the abundance of SO_2 on the VLA retrievals is a systematic offset in the derived temperature profile.

4.5. Comparison of Derived Temperature Profiles

Here we briefly compare and contrast the temperature profiles obtained in all three regions for a single assumed abundance of SO_2, namely 50 ppm. Figure 7 shows the three temperature profiles full scale, while Fig. 8 shows the difference between each retrieved profile and the PV sounder profile. The chief difference between the south high-latitude profile and the other two profiles is that the former is as much as 10 K warmer between
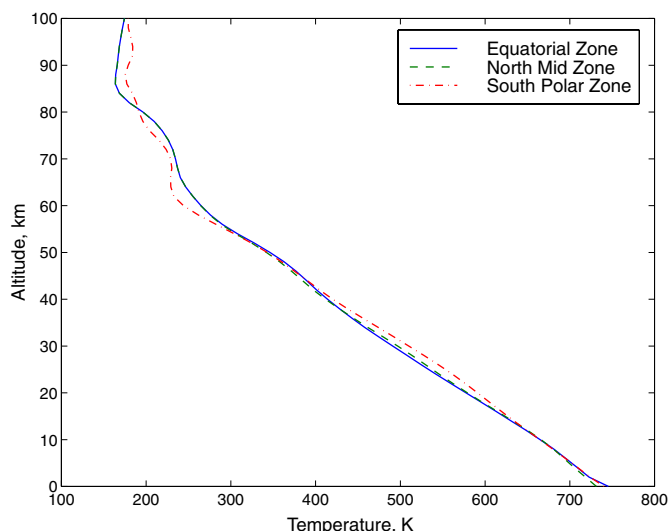
10 and 44 km. It is also as much as 25 K cooler between 50 and 80 km, although this is due principally to the initial seed profiles chosen for each region (see Appendix B). These differences are consistent with a Hadley cell exhibiting downwelling in the high-latitude regions, which warms the lower atmosphere via compression. The profiles from the eastern equatorial region and from the northern low-latitude region are within 5 K of each other over most of the altitude range between 5 and 50 km. This implies that the temperature profile of the atmosphere of Venus is remarkably uniform at latitudes below 45°, as was also observed by the PV probes.
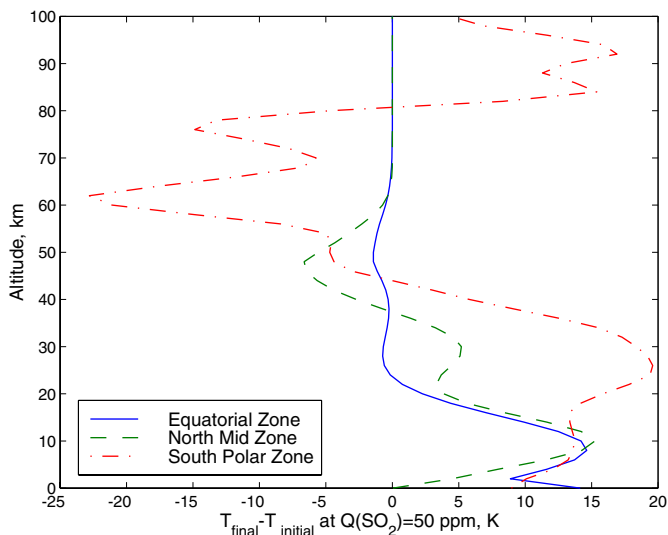

FIG. 8. Difference between retrieved profiles in all three regions and the PV sounder probe temperature profile.

4.6. Constraints on Sub-cloud SO₂ Abundance

Although we have not attempted to retrieve vertical profiles of SO_2, we can make a statement about the sub-cloud abundance supported by our data. Sub-cloud SO_2 abundances between 37 and 45 km inferred from observations of NIR SO_2 lines are $\sim$150 ppm (Bézard *et al.* 1993, Pollack *et al.* 1993). Abundances inferred from previous radio wavelength observations, however, are closer to 40 ppm assuming a uniform abundance below the cloud (Butler *et al.* 2002, Steffes *et al.* 1990). Table I contains a summary of the low-latitude, sub-cloud SO_2 abundances obtained from NIR and microwave observations and the assumed temperature profiles used in each investigation. We cannot discriminate completely between these two very different derived abundances, but we can say that our data are not consistent with a uniform abundance attaining the peak (150 ppm) obtained from NIR observations, when considering that these abundances were derived along with colder assumed atmospheric temperatures. We require either hotter temperatures or lower abundances of SO_2, or some combination of the two. However, the maps analyzed here can support as much as 100 ppm of SO_2 uniformly distributed below the cloud for a temperature profile similar to the COSPAR equatorial model down to 20 km. Below 20 km, the temperature profile needs to be $\sim$10 K warmer than the COSPAR model. Given that the PV probes did not return temperatures below 12 km, and that 100 ppm of SO_2 is within $\sim$1σ of both Bézard *et al.*'s (1993) and Pollack *et al.*'s (1993) results, this is not an unreasonable scenario. We note also that the absolute calibration of the VLA brightness temperature scale may play a significant role here. For example, if the maps are each cooled by 4%, good agreement is obtained for 130 ppm of SO_2 and a PV sounder-like temperature profile.

Higher abundances of SO_2 can be supported if we allow the SO_2 profile to vary below the cloud. Suppose that the SO_2 abundance profile is constant from the base of the cloud to 42 km, decaying linearly below this to 0 ppm at the surface, and decaying exponentially above 48 km as before. In this case, for $q_{SO_2} = 130$ ppm, the temperature profile required to fit the VLA maps is only $\sim$5 K warmer on average between 10 and 50 km than the temperature profile assumed by Bézard *et al.* (1993). However, as noted in Section 1, no plausible mechanism for establishing a gradient in the sub-cloud SO_2 abundance profile has been identified.

4.7. Discussion of the Low Sub-cloud H₂SO₄(g) Abundances at Low Latitudes

The low abundance of $H_2SO_4(g)$ retrieved at low latitudes (0 ± 2.5 ppm) is somewhat puzzling, given previous radio occultation studies and thermochemical, microphysical, and dynamical models for the formation of the lower cloud. While we cannot exclude the possibility that the low abundances obtained in this study are due to a systematic error in the absolute flux density scale of the VLA, the results have significant implications for our understanding of the altitude range of the return flow of the Hadley cell.

First, what does $q_{H_2SO_4}(z) = 0$ ppm mean in the context of the retrievals? Given the resolution of $\sim$12 km for $q_{H_2SO_4}(z)$, it is natural to wonder how significant these identically 0 ppm profiles are. The error bars of ± 2.5 ppm above 40 km coupled with the 12-km resolution imply that a value of 0 ppm at one particular altitude may be significantly less than the actual H_2SO_4 vapor content at that altitude. Moreover, if the vapor is confined to a layer whose vertical extent is much smaller than 12 km, it may be possible that the retrieval "misses" the presence of the layer entirely. This latter possibility may be investigated by examining the statistics of the total quantity of $H_2SO_4(g)$ recovered by the retrievals compared to the actual total content. We performed 100 Monte Carlo trials similar to those in Appendix B in which we restricted the sulfuric acid vapor to follow saturation to no more than 6 ppm, and then to drop to 0 ppm in the next 2-km bin below the peak. The trial temperature profiles were allowed to vary as described in Appendix B, affecting the saturation vapor abundance somewhat. The average total integrated $H_2SO_4(g)$ content of the test profiles was 13.1 ppm with over 98% of the vapor contained in three adjacent 2-km bins (the bin with the peak contained $\sim$66% of the total vapor). The results were striking. The total retrieved content exceeded 50% of the actual content of the trial profile in 90% of the cases. Moreover, 45% of the total vapor content was retrieved 95% of the time, and at least 25% of the total vapor content was retrieved in all 100 trials. Thus, we judge the $q_{H_2SO_4}(z) = 0$ ppm profiles retrieved in the east equatorial and the north low latitude regions to be highly significant, indeed.

With respect to previous measurements of the sub-cloud abundance of $H_2SO_4(g)$ at low latitudes, only a few radio occultations were performed by Mariner 5 and Mariner 10 that probed significantly below the base of the lower cloud. Both PVO and Magellan were unable to probe the lower latitudes with much sensitivity, or to probe altitudes significantly below the lower cloud base in the equatorial region, due to their polar-orbiting geometries. Although the abundance profile from Mariner 10 (adjusted as per Kolonder and Steffes 1998) peaks at 14 ± 3 ppm, there is significant scatter from point to point in the profile below the cloud base. A 3-km moving average of the profile would peak closer to 6 or 7 ppm. Given the 95% confidence interval of ± 2.5 ppm above 40 km (from Appendix B), we would have observed the effects of a peak of 6–7 ppm. This suggests that the sub-cloud abundance of sulfuric acid at low latitudes has decreased markedly since the Mariner 5 and Mariner 10 flybys.

The low abundance of $H_2SO_4(g)$ at low latitudes indicates a minimum altitude of 50 km for the base of the lower cloud, which typically extends from 48 to 51 km. Given the thermochemical, microphysical, and dynamic modeling of the lower cloud layer, then, it appears likely that the lower cloud layer was greatly diminished in its total mass and extent relative to its state prior to April 1996. Alternatively, the portion of the Venus atmosphere visible from Earth on April 5, 1996, was exceedingly patchy with respect to the mass of the lower cloud and the $H_2SO_4(g)$ reservoir below it. One dynamical mechanism explaining this would be a

decrease in the altitude level of the return flow of the Hadley cell. If the return flow's upper boundary drops much below 40 km, or if there is significant vertical mixing in the return flow among altitudes between 40 and 50 km and lower atmospheric regions, then the return flow would not contain much $H_2SO_4(g)$, as it is not present below 40 km in the first instance or would be thermochemically destroyed in the second.

5. CONCLUSIONS AND SUGGESTIONS FOR FUTURE WORK

To confirm the existence of vertical and horizontal variations in the abundances of both sulfuric acid vapor and sulfur dioxide in the atmosphere of Venus, a dual-frequency microwave observation of Venus was performed with the Very Large Array on April 5, 1996. The resulting VLA brightness temperature maps at 14.94 and 22.46 GHz display limb-darkening which is caused by the microwave effects of these sulfur compounds in the atmosphere of Venus and by spatial variations in the vertical temperature profile. They also display polar regions which are significantly darker than the equatorial regions. We jointly derived vertical profiles of $H_2SO_4(g)$ and temperature over a range of assumed sub-cloud SO_2 abundances for three separate regions of the disk of Venus. The uncertainties in the retrieved profiles were studied using Monte Carlo techniques, while the vertical resolution was examined using the theory of Rodgers (1976, 1990). The confidence in these retrievals must be tempered by their sensitivity to the absolute calibration scale of the VLA at these wavelengths. Future refinements in the flux scale would necessitate a reexamination of these maps and our findings.

In the east equatorial region and at northern low latitudes ($<45°$), the maps support a temperature profile 12–25 K warmer than the PV sounder probe profile below 40 km for an assumed SO_2 abundance of 150 ppm. In contrast, the combined NIR measurements obtained $\sim150 \pm 60$ ppm for SO_2 assuming a significantly cooler atmosphere similar to that measured by the PV sounder probe. The VLA maps support ≤100 ppm of SO_2 for a uniform sub-cloud abundance and a temperature profile consistent with the COSPAR equatorial model above 20 km. An SO_2 abundance of 100 ppm is within $1 - \sigma$ of the combined NIR measurements. In these regions the upper limit for the $H_2SO_4(g)$ abundance is 2.5 ppm. The low abundance of $H_2SO_4(g)$ at low latitudes indicates that the return flow of the Hadley cell was not providing significant amounts of this gas from high latitudes at the time of the VLA observations. Moreover, this result implies the absence or significant depletion of the lower cloud layer observed between 48 and 51 km prior to 1996.

In the southern high latitudes ($>45°$), the retrieved $H_2SO_4(g)$ abundance peaks near 8 ppm at 46 km, decaying rapidly below this altitude for assumed sub-cloud SO_2 abundances of 0–200 ppm. This is consistent with the series of radio occultation measurements made by the Magellan spacecraft in the early 1990s. The temperature profile is also consistent with the Magellan measurements, but only for relatively low sub-cloud

abundances of SO_2 (50 ppm). Higher abundances of SO_2 require significantly warmer temperatures than were measured by Magellan.

The results presented here represent an important method for studying the neutral atmosphere of Venus. While they do not have the resolution or sensitivity of the past radio occultation studies, they do illuminate the state of the atmosphere below 34 km, which is inaccessible to radio occultations. Over 76%, of the atmosphere (by surface area) is open to investigation by ground-based VLA observations, a region larely denied to the radio occultation studies performed by the near-polar-orbiting Magellan and PVO spacecraft. The VLA observations also provide important results for latitudes above 50°, albeit at lower spatial resolution than that obtainable by spacecraft occultation.

As indicated by the error analysis, the lowest temperature differences in the retrievals are obtained over the range of altitudes at which the peaks of the weighting functions are located (i.e., from ~10 to 30 km). For future work, obtaining maps at additional wavelengths would reduce the uncertainties outside of this interval. Achieving better resolution and lower uncertainties near the surface might be more difficult, however, as the simple uniform surface elevation and dielectric constant assumed for this work would no longer be valid. Butler *et al.* (2002) incorporate surface topography and dielectric properties directly into their radiative transfer model, demonstrating that this task is tractable, albeit at greater computational cost. In addition, conducting observations over one or more revolutions of the atmosphere of Venus (~5 days) would allow us to discriminate between features stationary with respect to the solar zenith angle and those which are rotating with the atmosphere. Conducting such observations in conjunction with infrared observations would reduce the systematic errors associated with the necessity to assume a given abundance of SO_2, as it would be provided by the latter measurements. We hope to perform future VLA observations of Venus at more than two wavelengths over longer integration intervals on a somewhat regular basis (perhaps once every three years) in conjunction with IR observations. This would enable us to observe potential long-term temporal variations in the abundances of sulfuric acid vapor and temperature both vertically and horizontally. These observations would give even greater insight into the global dynamical features and climatology of the atmosphere of Venus.

APPENDIX A

Retrieval of Atmospheric Profiles from the VLA Maps

In this appendix we describe our numerical approach to retrieving $T(z)$ and $q_{H_2SO_4}(z)$ from the dual-frequency brightness temperature maps obtained at the VLA. The method presented here can be extended in a straightforward manner to other multi-wavelength, spatially resolved microwave observations of Venus, or any other planet, assuming that scattering is negligible in the radiative transfer process.

In this approach, we assume that the abundance of SO_2 is given and fixed for a particular retrieval. This is necessary because the wavelength dependence of the absorptivity of SO_2 is the same as that for CO_2 except at very low pressures. Thus,

at microwave frequencies, it is not possible to separate the effects of the temperature profile of the atmosphere from variations in the vertical abundance of SO_2.

The quantities of interest are retrieved iteratively from the observed microwave emission maps. While the forward radiative transfer problem is well determined, the inverse problem of interest here is both ill-posed and nonlinear. To solve this problem we employ the Levenberg–Marquadt nonlinear minimization method along with zeroth-order regularization to stabilize the inversion (Press *et al.* 1996; pp. 799–806). In addition we apply several constraints described in Section 4.1 to speed convergence and increase the validity of the retrievals. The retrieved profiles are set up on a grid with 2-km vertical spacing, although they are interpolated onto a finer, 1-km vertical grid in the RTM. This spacing is sufficient given the results of the analysis presented in Appendix B showing that the vertical resolution of the retrieved profiles is on the order of 10 km.

At each step of the algorithm, we linearize the process of obtaining synthetic brightness temperature maps from the current $T(z)$ and $q_{H_2SO_4}(z)$ profiles. This is accomplished first by linearizing the equation of radiative transfer about the current profiles for a range of impact parameters from 0 km to the limb and then generating a set of gradient maps representing the partial derivative of each pixel value with respect to each quantity to be retrieved. Generating the partial derivative maps is straightforward since the conversion of $T_B(a)$ to a synthetic brightness temperature map is achieved by a sequence of linear operations. Thus, applying the same operations to the 1-D partial derivatives yields the appropriate gradient maps.

Let the column vector $\mathbf{B}$ represent the brightness temperature of the pixels of interest, and let the vector $\hat{\mathbf{B}}$ represent the model brightness temperature of these same pixels. The vector $\hat{\mathbf{B}}$ is determined by the parameter vectors for the temperature profile, $\mathbf{T}$, the sulfur dioxide abundance profile, $\mathbf{q_{SO_2}}$, and the sulfuric acid vapor abundance vector, $\mathbf{q_{H_2SO_4}}$. As only $\mathbf{T}$ and $\mathbf{q_{H_2SO_4}}$ are allowed to vary (and only at specific altitudes), we can combine them into one vector $\mathbf{u} = [\mathbf{T}^T, \mathbf{q_{H_2SO_4}}^T]^T$. Let $\mathbf{u}_0$ represent the initial or seed state of the model, and let $\mathbf{u}_i$ be the state of the model at step i. Expanding $\mathbf{B}$ in a Taylor series about a particular state $\mathbf{u}_i$ (with corresponding model $\mathbf{B}_i$) we obtain

$$\hat{\mathbf{B}} = \mathbf{B}_i + \mathbf{A} \cdot \Delta\mathbf{u}, \qquad (A1)$$

where $\mathbf{A}$ is the Jacobian of $\hat{\mathbf{B}}$ with respect to $\mathbf{u}_i$, which contains the unknown temperatures and sulfuric acid vapor abundances. We define the error function, E, as the sum of the χ^2 error and an additional regularization term,

$$E = (\mathbf{T_B} - \hat{\mathbf{T}_B})^T \cdot \mathbf{C}^{-1} \cdot (\mathbf{T_B} - \hat{\mathbf{T}_B}) + (\mathbf{u} - \mathbf{u}_0)^T \cdot \mathbf{H} \cdot (\mathbf{u} - \mathbf{u}_0), \qquad (A2)$$

where $\mathbf{C}$ is the covariance matrix of the brightness temperature measurements. Since $\mathbf{C}$ is singular for the VLA maps, we replace it with a diagonal matrix whose entries are the uncertainties in the pixel brightness temperatures. In other words, we treat the measurement errors as uncorrelated, an approach that Rodgers (1990) argues is conservative. The regularization matrix $\mathbf{H}$ has the following structure:

$$\mathbf{H} = \begin{bmatrix} 10\,\mathbf{I}_{n_T} & \mathbf{0} \\ \mathbf{0} & \mathbf{D} \end{bmatrix}. \qquad (A3)$$

Here, $\mathbf{I}_{n_T}$ is a 38 × 38 identity matrix and $\mathbf{D}$ is a 15 × 15 diagonal matrix with entries given by

$$D(z) = \begin{cases} 10, & z \geq 40 \text{ km} \\ 100(40 - z)^2, & z < 40 \text{ km}, \end{cases} \qquad (A4)$$

where z is altitude. This form for $\mathbf{D}$ severely penalizes nonzero abundances of $H_2SO_4(g)$ below 40 km.

We do not claim that the particular form for the regularization term, $\mathbf{H}$, in Eq. (A3) is optimal. It was obtained by performing a large number of Monte Carlo runs for first as well as for zeroth order of regularization and for different scale factors for the matrix $\mathbf{H}$. This effort resulted in the particular $\mathbf{H}$ given by

(A3) that achieved the smallest fitting errors for the limited region we explored of the vast parameter space.

The step to take from the current solution $\mathbf{u}_i$ to the next iteration is given by the following:

$$\mathbf{u}_{i+1} = \mathbf{u}_i + (\mathbf{A}^T \cdot \mathbf{C}^{-1} \cdot \mathbf{A} + \mathbf{H} + \lambda\mathbf{I})^{-1}$$
$$\cdot [\mathbf{A}^T \cdot \mathbf{C}^{-1} \cdot (\mathbf{B} - \hat{\mathbf{B}}) + \mathbf{H} \cdot (\mathbf{u}_i - \mathbf{u}_0)], \qquad (A5)$$

The parameter $0 < \lambda < \infty$ is the weight in the Levenberg–Marquadt algorithm that elegantly combines two approaches for minimizing a nonlinear function of several variables: the steepest descent method and the inverse Hessian method (Press *et al.* 1996). The value of λ is decreased if the trial solution improves the total difference in (A2); otherwise it is increased until E decreases or the convergence criterion is satisfied (see Press *et al.* (1996) for additional details).

This method is rather efficient. Convergence is generally achieved in less than 10 iterations, requiring only a few minutes on a desktop personal computer when techniques for accelerating the calculations in the RTM and the conversion from 1-D quantities to 2-D quantities are used (as discussed in Appendix C).

APPENDIX B

Error Analysis

This appendix describes our efforts to quantify the stochastic uncertainties in the temperature and $H_2SO_4(g)$ profiles derived from the VLA brightness temperature maps. We also present the results of a study of the resolution of the retrievals. In principle, these uncertainties could have been determined from the linearized inverse problem using the standard propagation of errors. However, given the nonlinear nature of the radiative transfer process and the additional constraints placed on the retrieved sulfuric acid vapor profiles, we felt it was better to adopt a Monte Carlo approach. In addition, this process provided a method for establishing the appropriate value for the weight given to the regularization matrix, $\mathbf{H}$ (see Eq. (A3)). This approach consisted of generating synthetic brightness temperature maps at both observed frequencies, adding simulated measurement noise consistent with the actual observations, and attempting to recover the temperature and sulfuric acid vapor profiles used to generate the noise-corrupted, synthetic maps.

The target profile for $H_2SO_4(g)$ was modified randomly for each run. In this case, $q_{H_2SO_4}(z)$ was given by a Gaussian with FWHM of 9.1 km and peak amplitude drawn from a uniform distribution between 0 and 5 ppm. Each target $T(z)$ was obtained by perturbing the PV sounder probe profile, T_{PVS}, in the following manner. First, a random Gaussian profile was added to $T_{PVS}(z)$. This Gaussian had a FWHM of 25 km and an amplitude drawn from a zero-mean normal distribution with a standard deviation of 5 K. Next, a fifth-order polynomial was added to $T(z)$ below 60 km. This polynomial was constrained to be zero at 60 km and to be one at 0 km and to have one root in its first derivative at 0 km and two roots at 60 km. The polynomial was scaled by a value drawn from a zero-mean Gaussian distribution with a standard deviation of 10 K.

For each $T(z)$ and $q_{H_2SO_4}(z)$ constructed, a set of synthetic maps was generated using the RTM and the process described in Section 3. We generated noise maps by convolving arrays of white Gaussian noise of appropriate variance with the Gaussian CLEAN beams to obtain noise with similar spatial correlation structure as in the actual maps. The noise maps were added to the noise-free, synthetic brightness temperature maps. The algorithm of Appendix A was used to determine the solution profiles for each set of synthetic maps. A fixed abundance of SO_2 of 150 ppm was used both to generate the synthetic target maps and to retrieve the profiles. We performed 100 runs using the pixels from the equatorial region discussed in Section 4.2. The differences between the retrieved profiles and the target profiles established the stochastic uncertainties in the retrievals.

The approach taken here can be considered to be quasi-Bayesian in the following sense. The Bayesian approach would be to vary the target profiles over the given prior distributions and to study the distributions of the resulting fitting errors. Our process is similar except that we have adopted somewhat arbitrary
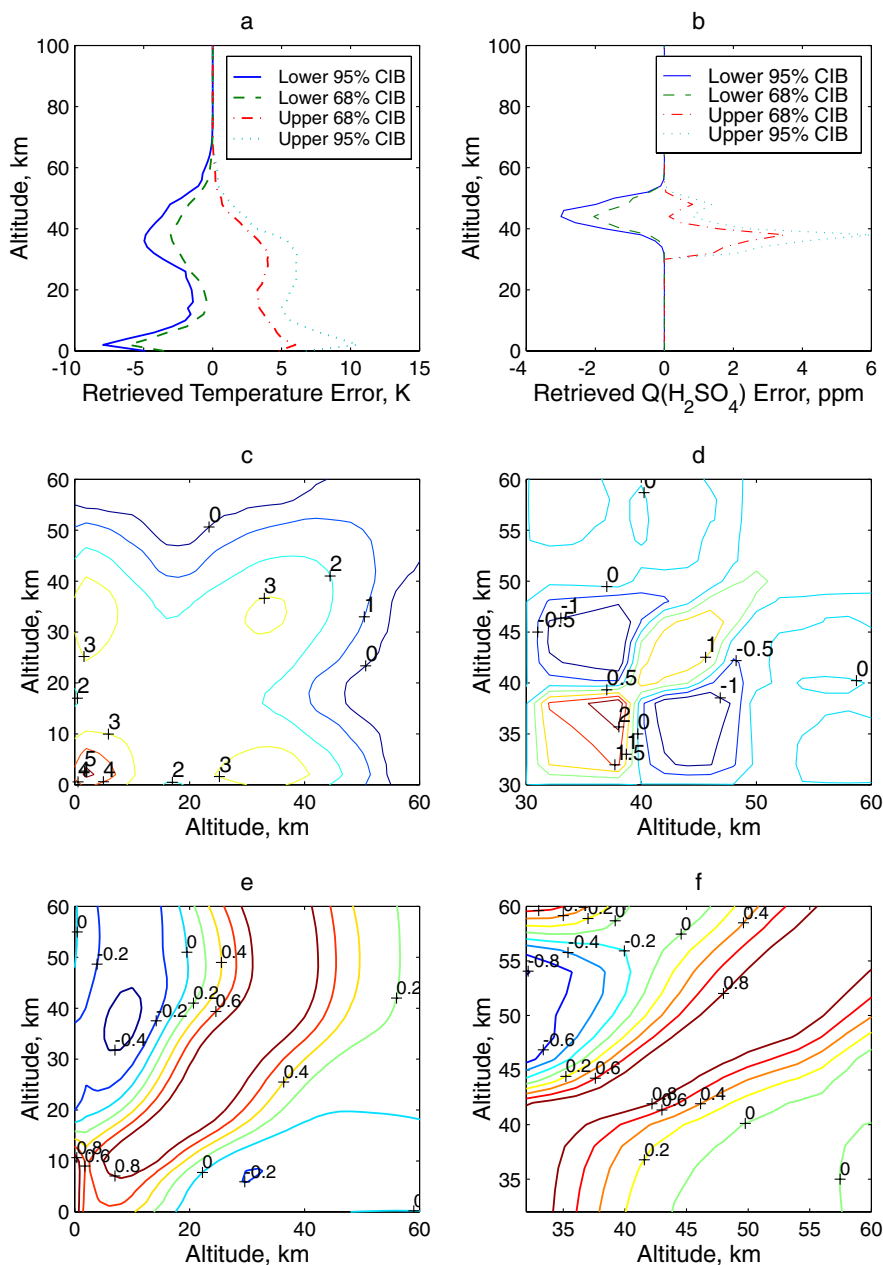
FIG. 9. Error analysis for the retrieved profiles. (a) Bounds of 68 and 95% confidence intervals obtained from 100 Monte Carlo simulations for temperature retrievals in the equatorial region. (b) Bounds of 68 and 95% confidence intervals obtained from 100 Monte Carlo simulations for $H_2SO_4(g)$ abundance profile retrievals in the equatorial region. (c) Contour map of the root variance of uncertainties in temperature retrievals obtained from 100 Monte Carlo runs. The signs of the correlations are preserved in this map. The diagonal represents the rms uncertainties of the retrievals at each probed altitude. (d) Contour map of the root variance of uncertainties in sulfuric acid vapor retrievals obtained from 100 Monte Carlo runs. The signs of the correlations are preserved in this map. The diagonal represents the rms uncertainties of the retrievals at each probed altitude. (e) Contour map of the "averaging kernels" for the retrievals of the temperature profile. The kernels are normalized for each altitude to be one at the altitude that contributes the most weight. The normalized kernel for each altitude is a horizontal section of the map given by the vertical axis. (f) Contour map of the "averaging kernels" for the retrievals of $H_2SO_4(g)$ abundance. The kernels are normalized for each altitude to be one at the altitude that contributes the most weight. The normalized kernel for each altitude is a horizontal section of the map given by the vertical axis.

prior distributions and are not using a Bayesian estimation procedure to obtain the retrievals. On the other hand, this approach provides information of the general ability of the retrieval algorithm to accurately retrieve an arbitrary set of profiles. In contrast, the standard propagation of errors establishes the ability of an algorithm to derive one particular atmospheric model in the presence of stochastic uncertainties.

Figure 9a shows the 68 and 95% confidence intervals for the retrieved temperature profiles. The 68% confidence interval bounds are within -3 K and $+4$ K everywhere except below 10-km altitude. The 95% confidence interval bounds are within -5 K and $+6$ K above 10-km altitude. Figure 9c shows the square root of the variance matrix of the temperature uncertainties multiplied by the sign of the variance matrix to preserve negative correlations. The diagonal is

the rms uncertainty at each altitude. Not surprisingly, the lowest uncertainties (≤ 3 K) occur between ~ 10 and ~ 30 km, the region with the densest distribution of high weighting function values, as exhibited in Figs. 3a and 3b.

The confidence intervals for the retrieved H_2SO_4(g) profiles are given in Fig. 9b. Here, the 68% confidence interval bounds are contained between -2 and $+3.5$ ppm while the 95% confidence interval is confined between -3 and $+6$ ppm. It is important to note that the constraints on the sulfuric acid vapor profile lead to a systematic positive peak in the uncertainties below 40 km, where little H_2SO_4(g) is expected. Above 40 km the uncertainties at 68 and 95% confidence are less than 1.5 and 2.5 ppm, respectively. Figure 9d shows the square root of the variance matrix of the uncertainties in the retrieved sulfuric acid vapor profiles multiplied by the sign of the variance matrix elements. The uncertainties below 40 km are negatively correlated with the uncertainties between 40 and 50 km, indicating that a spurious layer of H_2SO_4(g) below 40 km occurs when too little vapor is inferred in the immediate sub-cloud region. This implies that better retrievals might result if we constrained the H_2SO_4(g) to be zero below 40 km, knowing that it should, indeed, decay rapidly below this altitude.

To study the resolution of the retrieved profiles we applied the theory developed by Rodgers (1976, 1990) to obtain the "averaging kernels" of the retrieval algorithm. Basically, if $\hat{\mathbf{u}}$ is the retrieved profile, and $\mathbf{u}$ is the true state of the atmosphere, then the transformation from $\mathbf{u}$ to $\hat{\mathbf{u}}$ is given in terms of the discussion in Appendix A by

$$\hat{\mathbf{u}} = \mathbf{K} \cdot \mathbf{u} = (\mathbf{A}^T \cdot \mathbf{A} + \mathbf{B})^{-1} \cdot (\mathbf{A}^T \cdot \mathbf{A}) \cdot \mathbf{u}. \tag{B1}$$

The ith row of $\mathbf{K}$ reveals the contribution from the true state at each altitude to the solution's ith element. The FWHM of the averaging kernels, if they are unimodal, can be interpreted as the resolution of the retrieval as a function of altitude. Figures 9e and 9f are contour maps of the "averaging kernels" for $T(z)$ and $q_{H_2SO_4}(z)$ for the equatorial region. The averaging kernels for the other two regions are similar to these. The resolution of the temperature retrievals is approximately 20 km. We also observe that the retrievals do not consider temperature information much above 50 km. The values above 50 km are weighted averages of the temperature profile below this level. The averaging kernels serve to provide a smooth transition from the initial temperature profile in the region of the atmosphere poorly probed by our data (above 50 km) and that well probed by our data (below 40 km). The contour map for $\mathbf{K}$ for H_2SO_4(g) given in Fig. 9f indicates a resolution of about 12 km. Equation (B1) does not take nonlinear constraints for $q_{H_2SO_4}(z)$ into account, however, so the true resolution is likely somewhat finer than indicated by this analysis.

APPENDIX C

Acceleration of the Numerical Calculations

This appendix describes the methodology used to accelerate the radiative transfer calculations and the generation of synthetic brightness temperature maps. Our assumption of local spherical symmetry and a uniform surface altitude and dielectric allows for extremely efficient generation of the synthetic brightness temperature maps and the gradient maps required for data inversion.

First we note that for a spherically symmetric atmosphere modeled as a concentric set of uniform shells with respect to both absorptivity and refractivity it is not necessary to actually trace rays. The differential equation of a light ray under geometric optics can be integrated in closed form over each layer to obtain the ray-path-integrated absorption in each layer as a function of the impact parameter, a. Also, for limb-sounding rays the deepest point of penetration is obtained by noting that everywhere along the ray $a = n\,r\,\sin\psi$, where a is the ray impact parameter, r is the radius, n is the index of refraction, and ψ is the inclination angle along the ray (Born and Wolf 1959). Thus, the deepest altitude penetrated by a given ray is that at which $r = a/n$, since at the point of closest approach $\psi = \pi/2$. Moreover, for rays that strike the surface this relationship provides an immediate determination of the emission angle at the surface.

Another method for improving the efficiency is the use of 2-D interpolation over a PT grid to compute the opacity of SO_2 from precomputed values using the

numerically costly, full Ben Reuven formalism. The most significant gain in efficiency, however, is the reduction of the 2-D integral implied by the convolution of the infinite-resolution brightness temperature map, $B'_\nu(a)$, with the Gaussian CLEAN beam, $G_\nu(x, y)$, to obtain a map, $B''_\nu(a)$, at the same resolution as the actual VLA brightness temperature maps,

$$B''_\nu(a) = B'_\nu(x, y) * G_\nu(x, y), \tag{C1}$$

where $G_\nu(x, y) = (\ln(2)/\pi HWHM^2)\exp(-\ln 2\,(x^2 + y^2)/HWHM^2)$ is the 2-D Gaussian beam with half width half maximum $HWHM$. The 2-D convolution in Eq. (C1) can be reduced to the 1-D integral

$$B''(a) = \frac{2\ln 2}{HWHM^2}\int_0^R B'_\nu(a)\exp\left[\frac{-\ln 2(x^2 + a^2)}{HWHM^2}\right]I_0\left(\frac{2\ln 2\,a\,x}{HWHM^2}\right)dx, \tag{C2}$$

where R is the radius of Venus including the atmosphere (6152 km) and I_0 is the modified Bessel function of zeroth order (D. Muhleman, personal communication). Now if the set of impact parameters for which the RTM is evaluated remains fixed and if $B'(a)$ is modeled as a piecewise polynomial over the underlying grid, Eq. (C2) can be evaluated rapidly for different atmospheric models. This is accomplished by precomputing the integral in (C2) over each interval in normalized impact parameter (rather than over the entire disk) for each polynomial term, from the constant term up to the order of polynomial to be used and storing the results in a matrix; i.e.,

$$\mathbf{W}_{ij} = \frac{2\ln 2}{HWHM^2}\int_{a_i}^{a_{i+1}} x^{j+1}\exp\left[\frac{-\ln 2(x^2 + a^2)}{HWHM^2}\right]I_0\left(\frac{2\ln 2\,a\,x}{HWHM^2}\right)dx, \tag{C3}$$

where $i \in \{0, \ldots, N\}$, $j \in \{0, \ldots, 3\}$. Equation (C2) then reduces to the product of the precomputed quadrature weight matrix, $\mathbf{W}_{ij}$, and the matrix of piecewise-polynomial coefficients for the piecewise-polynomial model of $B'_\nu(a)$.

ACKNOWLEDGMENTS

REFERENCES

Berge, G. L., and E. W. Greisen 1969. High-resolution interferometry of Venus at 3.12-cm wavelength. *Astrophys. J.* **156**, 1125–1134.

Bertaux, J., T. Widemann, A. Hauchecorne, V. I. Moroz, and A. P. Ekonomov 1996. VEGA-1 and VEGA-2 entry probes: An investigation of local UV absorption (220–400 nm) in the atmosphere of Venus (SO_2, aerosols, cloud structure). *J. Geophys. Res.* **101**, 12709–12745.

Bézard, B., C. de Bergh, B. Fegley, J.-P. Maillard, D. Crisp, T. Owen, J. B. Pollack, and D. Grinspoon 1993. The abundance of sulfur dioxide below the clouds of Venus. *Geophys. Res. Lett.* **20**, 1587–1590.

Born, M., and E. Wolf 1959. *Principles of Optics*. Pergamon Press, New York.

Butler, B. J., and T. S. Bastian 1999. Solar System objects. In *Synthesis Imaging in Radio Astronomy II* (G. B. Taylor, C. L. Carilli, and R. A. Perley, Eds.), pp. 625–656. Astron. Soc. of the Pac. Conf. Ser., San Francisco.

Butler, B. J., P. G. Steffes, S. H. Suleiman, M. A. Kolodner, and J. M. Jenkins 2001. Accurate and consistent microwave observations of Venus and their implications. *Icarus* **154**, 226–238.

Clark, B. G. 1980. An efficient implementation of the algorithm CLEAN. *Astron. Astrophys.* **89**, 377–378.

Clark, B. G., and A. D. Kuzmin 1965. The measurement of the polarization and brightness distribution of Venus at 10.6-cm wavelength. *Astrophys. J.* **142**, 23–44.

Cornwell, T., and E. B. Fomalont 1999. Self-calibration. In *Synthesis Imaging in Radio Astronomy II* (G. B. Taylor, C. L. Carilli, and R. A. Perley, Eds.), pp. 187–199. Astron. Soc. of the Pac. Conf. Ser., San Francisco.

Cornwell, T., R. Braun, and D. S. Briggs 1999. Deconvolution. In *Synthesis Imaging in Radio Astronomy II* (G. B. Taylor, C. L. Carilli, and R. A. Perley, Eds.), pp. 151–170. Astron. Soc. of the Pac. Conf. Ser., San Francisco.

Essen, L., and K. D. Froome 1951. The refractive indices and dielectric constants of air and its principle constituents at 24000 Mc/s. *Proc. Phys. London B* **64**, 862–875.

Fahd, A. K. 1992. *Study and Interpretation of the Millimeter-Wave Spectrum of Venus*. Thesis, Georgia Institute of Technology, Atlanta.

Fjeldbo, G., and A. J. Kliore 1971. The neutral atmosphere of Venus as studied with the Mariner V radio occultation experiments. *Astron. J.* **76**, 123–140.

Hinson, D. P., and J. M. Jenkins 1995. Magellan radio occultation measurements of atmospheric waves on Venus. *Icarus* **114**, 310–327.

Ho, W., I. A. Kaufman, and P. Thaddeus 1966. Laboratory measurements of microwave absorption models of the atmosphere of Venus. *J. Geophys. Res.* **71**, 5091–5108.

Högbom, J. A. 1974. Aperture synthesis with a non-regular distribution of interferometer baselines. *Astron. Astrophys. Suppl.* **15**, 417–426.

Howard, H. T., and 19 colleagues 1974. Venus: Mass, gravity field, atmosphere and ionosphere as measured by the Mariner 10 dual-frequency radio system. *Science* **183**, 1297–1301.

Imamura, T., and G. L. Hashimoto 1998. Venus cloud formation in the meridional circulation. *J. Geophys. Res.* **103**, 31349–31366.

James, E. P., O. B. Toon, and G. Schubert 1997. A numerical microphysical model of the condensational Venus cloud. *Icarus* **129**, 147–171.

Jenkins, J. M., and D. P. Hinson 1997. Magellan radio occultation studies of Venus' atmosphere (1991–1994). *Bull. Am. Astron. Soc.* **29**, 1044 (abstract).

Jenkins, J. M., and P. G. Steffes 1991. Results for 13-cm absorptivity and H_2SO_4 abundance profiles from the season 10 (1986) Pioneer Venus Orbiter radio occultation experiment. *Icarus* **90**, 129–138.

Jenkins, J. M., P. G. Steffes, D. P. Hinson, J. D. Twicken, and G. L. Tyler 1994. Radio occultation studies of the Venus atmosphere with the Magellan spacecraft. 2. Results from the October 1991 experiments. *Icarus* **110**, 79–94.

Kliore, A. J., and I. R. Patel 1980. Vertical structure of the atmosphere of Venus from Pioneer Venus Orbiter radio occultations. *J. Geophys. Res.* **85**, 7957–7962.

Knollenberg, R. G., and D. M. Hunten 1980. The microphysics of the clouds of Venus—Results of the Pioneer Venus particle size spectrometer. *J. Geophys. Res.* **85**, 8039–8058.

Kolodner, M. A., and P. G. Steffes 1998. The microwave absorption and abundance of sulfuric acid vapor in the Venus atmosphere based on new laboratory measurements. *Icarus* **132**, 151–169.

Kolosov, M. A., O. I. Yakovlev, A. I. Efimov, A. G. Pavelyev, and S. S. Matyugov 1979. Radio occultation of the Venusian atmosphere and bistatic radiolocation of the surface of Venus using the Venera-9 and Venera-10 satellites. *Radio Sci.* **14**, 163–173.

Krasnopolsky, V. A., and J. B. Pollack 1994. H_2O–H_2SO_4 system in Venus' clouds and OCS, CO, and H_2SO_4 profiles in Venus' troposphere. *Icarus* **109**, 58–78.

Limaye, S. S., C. J. Grund, and S. P. Burre 1982. Zonal mean circulation at the cloud level on Venus: Spring and Fall 1979 OCPP observations. *Icarus* **51**, 416–439.

Lipa, B., and L. Tyler 1979. Statistical and computational uncertainties in atmospheric profiles from radio occultation: Mariner 10 at Venus. *Icarus* **39**, 192–208.

Matyugov, S. S., O. I. Yakovlev, and V. N. Gubenko 1990. *Sulfuric Acid in Venusian Atmosphere Determined from Radio Opacity Data*. JPRS Report: Science and Technology. USSR: Space 35 pp. (see N91-20154 12-12). Transl. into English from *Kosmicheskiye Issledovaniya* **28**, 277–281.

Muhleman, D. O., G. S. Orton, and G. L. Berge 1979. A model of the Venus atmosphere from radio, radar, and occultation observations. *Astrophys. J.* **234**, 733–745.

Napier, P. J. 1999. The primary antenna elements. In *Synthesis Imaging in Radio Astronomy II* (G. B. Taylor, C. L. Carilli, and R. A. Perley, Eds.), pp. 37–56. Astron. Soc. of the Pac. Conf. Ser., San Francisco.

Perley, R. A. 1999. High dynamic range imaging. In *Synthesis Imaging in Radio Astronomy II* (G. B. Taylor, C. L. Carilli, and R. A. Perley, Eds.), pp. 275–299. Astron. Soc. of the Pac. Conf. Ser., San Francisco.

Pettengill, G. H., P. G. Ford, and R. J. Wilt 1992. Venus surface radiothermal emission as observed by Magellan. *J. Geophys. Res.* **97**, 13091–13102.

Pollack, J. B., J. B. Dalton, D. Grinspoon, R. B. Wattson, R. Freedman, D. Crisp, A. Allen, B. Bézard, C. de Bergh, L. P. Giver, Q. Ma, and R. Tipping 1993. Near infrared light from Venus' nightside: A spectroscopic analysis. *Icarus* **103**, 1–42.

Press, W. H., S. A. Teukolsky, W. T. Vetterling, and B. P. Flannery 1996. *Numerical Recipes in FORTRAN: The Art of Scientific Computing*, Vol. 1 of Fortran Numerical Recipes. Cambridge Univ. Press, New York.

Rodgers, C. 1976. Retrieval of atmospheric temperature and composition from remote measurements of thermal radiation. *Rev. Geophys. Space Phys.* **14**, 609–624.

Rodgers, C. 1990. Characterization and error analysis of profiles retrieved from remote sounding measurements. *J. Geophys. Res.* **95**, 5587–5595.

Rossow, W. B., A. D. Del Genio, S. S. Limaye, L. D. Travis, and P. H. Stone 1980. Cloud morphology and motions from Pioneer Venus images. *J. Geophys. Res.* **85**, 8107–8128.

Seiff, A. 1983. Models of Venus's atmospheric structure. In *Venus* (D. M. Hunten, L. Colin, T. M. Donahue, and V. I. Moroz, Eds.), pp. 1045–1048. Univ. of Arizona Press, Tuscon.

Seiff, A., B. D. Kink, R. E. Young, R. C. Blanchard, J. T. Findlay, G. M. Kelly, and S. C. Sommer 1980. Measurements of thermal structure and thermal contrasts in the atmosphere of Venus and related dynamical observation: Results from the four Pioneer Venus probes. *J. Geophys. Res.* **85**, 7903–7933.

Seiff, A., J. T. Schofield, A. J. Kliore, F. W. Taylor, S. S. Limaye, H. E. Rivercomb, L. A. Sromovsky, V. V. Kerzhanovich, V. I. Moroz, and M. Ya. Marov 1986. Models of the structure of the atmosphere of Venus from the surface to 100 kilometer altitude. In *The Venus International Reference Atmosphere* (A. J. Kliore, V. I. Moroz, and G. M. Keating, Eds.), pp. 3–58. Pergamon Journals, Oxford.

Sinclair, A. C. E., J. P. Basart, D. Buhl, and W. A. Gale 1972. Precision interferometric observations of Venus at 11.1-centimeter wavelength. *Astrophys. J.* **175**, 555–572.

Steffes, P. G., and V. R. Eshleman 1981. Laboratory measurements of the microwave opacity of sulfur dioxide and other cloud-related gases under simulated conditions for the middle atmosphere of Venus. *Icarus* **48**, 180–187.

Steffes, P. G., M. J. Klein, and J. M. Jenkins 1990. Observations of the microwave emission of Venus from 1.3 to 3.6 cm. *Icarus* **85**, 83–92.

Suleiman, S. H., M. A. Kolodner, and P. G. Steffes 1996. Laboratory measurement of the temperature dependence of gaseous sulfur dioxide (SO_2) microwave absorption with application to the Venus atmosphere. *J. Geophys. Res.* **101**, 4623–4635.

Thompson, A. R., J. M. Moran, and G. W. Swenson Jr. 2001. *Interferometry and Synthesis in Radio Astronomy,* 2nd ed. Wiley, New York.

Yakovlev, O. I., S. S. Matyugov, and V. N. Gubenko 1991. Venera-15 and-16 middle atmosphere profiles from radio occultations: Polar and near-polar atmosphere of Venus. *Icarus* **94**, 493–510.